

# Magnetic and Plasmonic Contrast Agents in Optical Coherence Tomography

Amy L. Oldenburg, Richard L. Blackmon, and Justin M. Sierchio

(Invited Paper)

**Abstract**—Optical coherence tomography (OCT) has gained widespread application for many biomedical applications, yet the traditional array of contrast agents used in incoherent imaging modalities do not provide contrast in OCT. Owing to the high biocompatibility of iron oxides and noble metals, magnetic and plasmonic nanoparticles, respectively, have been developed as OCT contrast agents to enable a range of biological and pre-clinical studies. Here, we provide a review of these developments within the past decade, including an overview of the physical contrast mechanisms and classes of OCT system hardware add-ons needed for magnetic and plasmonic nanoparticle contrast. A comparison of the wide variety of nanoparticle systems is also presented, where the figures of merit depend strongly upon the choice of biological application.

**Index Terms**—Contrast agents, magnetomotive, optical coherence tomography, plasmonic nanoparticles, superparamagnetic iron oxides.

## I. INTRODUCTION

OPTICAL coherence tomography (OCT), first reported in 1991 [1], has become widely adapted particularly for retinal imaging [2] and other ophthalmic applications [3], with emerging applications in coronary artery imaging [4], surgical guidance [5], and endoscopic imaging of the gastro-intestinal tract [6], [7] and upper airways [8]. OCT operates on the principle of low-coherence gating to provide a depth-resolved image of light scattering within biological tissue [9]. Light scattering, in general, is caused by refractive index heterogeneities on the scale of the wavelength of the probing light ( $\lambda$ ), which means that cells and subcellular objects such as nuclei and mitochondria tend to provide OCT contrast [10]. This mechanism of contrast allows one to distinguish different cell layers within the human retina [11], sites of atherosclerotic plaque within the coronary artery [12], as well as blood flow for angiography [13]. However, it is also somewhat limited for applications such as

cancer detection, where the speckled features of normal and cancer tissue can appear very similar [14].

In order to widen the application space of OCT, there has been much effort to develop contrast agents and associated imaging methods [15], [16]. Because OCT only senses coherently backscattered light, it cannot detect light from traditional incoherent (fluorescent) probes used widely in microscopy. To develop an effective contrast agent probe for OCT, it must provide a signal that is distinct from that of the tissue surrounding it. In this paper, we discuss two highly successful classes of contrast agents: magnetic contrast agents that, when interrogated with a magnetic field, provide a unique motion signal, and plasmon-resonant contrast agents that exhibit extremely high optical cross-sections, offering a variety of optical effects that can be exploited for sensing within tissue. In many applications such as cancer diagnostics, effective targeting of these agents by bioconjugation or the enhanced permeability and retention effect is needed, and the reader is directed to reviews for more detailed information about targeting moieties [17], [18]. Also, magnetic and plasmonic nanoparticles are by no means the only methods for OCT contrast enhancement, and the reader is directed to review articles that cover a broader range of development [16], [19], [20].

## II. MAGNETOMOTIVE OCT: THEORY AND PRACTICE

The magnetic volume susceptibility at zero magnetic field,  $\chi(B=0)$ , quantifies the rate of change in the magnetization of a material as the magnetic flux density,  $B$ , is increased. Biological tissues are relatively non-magnetic, that is,  $\chi$  is on the order of  $-10^{-5}$ , and is dominated by that of water [21]. In comparison, magnetic iron oxides (MIOs) can exhibit  $\chi \sim 1$ , or  $10^5$  stronger than that of tissue. Thus,  $\chi$  can provide an effective contrast mechanism for magnetic particle imaging. Because OCT is particularly sensitive to motion, with phase-resolved OCT providing displacement resolution in the picometer range [22], magnetomotive OCT (MMOCT) exploits the motion of magnetic nanoparticles induced by an applied magnetic field (see Fig. 1). This is known as the magnetic gradient force effect:

$$\vec{F} = \frac{V(\chi - \chi_{\text{med}}) \nabla |\vec{B}|^2}{2\mu_0} \quad (1)$$

where  $F$  is the force acting on the MIO with susceptibility  $\chi$  within its surrounding medium,  $\chi_{\text{med}}$ ,  $B$  is the magnetic flux density,  $V$  is the MIO volume, and  $\mu_0$  is the vacuum permeability. Interestingly, the force acting on particles with

Manuscript received October 16, 2015; revised April 6, 2016; accepted April 7, 2016. This work was supported in part by the National Science Foundation under Grant CBET 1351474, and in part by the National Institutes of Health under Grants R21 HL 119928 and R21 HL 111968. Additional information can be found at <http://user.physics.unc.edu/~aold/>.

A. L. Oldenburg is with the Department of Physics and Astronomy, Department of Biomedical Engineering, Biomedical Research Imaging Center, University of North Carolina at Chapel Hill, Chapel Hill, NC 27599-3255 USA (e-mail: aold@physics.unc.edu).

R. L. Blackmon and J. M. Sierchio are with the Department of Physics and Astronomy, University of North Carolina at Chapel Hill, Chapel Hill, NC 27599-3255 USA (e-mail: rlblackm@email.unc.edu; jmsierch@email.unc.edu).

Color versions of one or more of the figures in this paper are available online at <http://ieeexplore.ieee.org>.

Digital Object Identifier 10.1109/JSTQE.2016.2553084

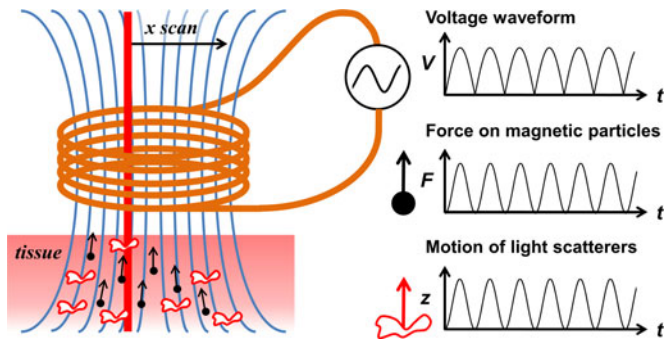


Fig. 1. Concept diagram of sinusoidal MMOCT. Tissue containing MNPs (black dots) is placed in the fringe field (blue lines) of a solenoid, while the OCT imaging beam scans through its bore. A square-root sinusoidal voltage applied to the solenoid produces a pure sinusoidal force on MNPs directed along the field gradient. OCT detects the resulting axially-directed motion ( $z$ ) of light-scattering structures within the tissue that are mechanically coupled to the MNP motion.

$\chi > 0$  (paramagnetic) always points toward the electromagnet, irrespective of the polarity of the  $B$  field.

MIOs are a natural choice as MMOCT contrast agents because iron is already metabolized within the human body in large quantities, and iron oxide nanoparticles have already been in use as MRI contrast agents with few side effects [23]. There are two magnetic crystalline forms of iron oxide:  $\gamma$ - $\text{Fe}_2\text{O}_3$  (maghemite) and  $\text{Fe}_3\text{O}_4$  (magnetite), which can often be produced by the same synthesis methods and can be difficult to distinguish between due to similar X-ray diffraction and magnetic properties [24]. Thermodynamically, magnetite slowly oxidizes to maghemite, then eventually to hematite ( $\alpha$ - $\text{Fe}_2\text{O}_3$ , or rust) [25].

Interestingly, the figures of merit for an OCT contrast agent are different than for MRI contrast. In MRI, MIOs must be small in order to maximize surface area contact with adjacent water molecules, whose magnetic resonance is shifted by the local particle magnetization [26]. In OCT, MIOs must maximize their motion via Eqn. (1), which suggests a large particle volume,  $V$ . However, there are two practical limits to the size of MNPs: a) if particles are too large to be administered to the imaging target (e.g., into small capillaries or by diffusion through tissue), and b) if particles become significantly ferromagnetic such that they irreversibly aggregate under an applied magnetic field. Superparamagnetic iron oxides (SPIOs) are typically desired because they maintain strong magnetic susceptibility while lacking remanent magnetization. Thus, MMOCT contrast agents tend to have MIO cores between  $\sim 10$ – $50$  nm, although larger particle clusters [27] or novel ferrofluid-filled microspheres [28] have been developed for certain applications.

Importantly, MIOs are optically absorbing, appearing almost completely black in color. Thus, it is not possible to use OCT to directly sense their magnetic gradient-driven motion (magneto-motion). It is only in their coupling with adjacent light scattering structures within the tissue that they can be detected (see Fig. 1). MIOs free in solution (such as a blood vessel) will exhibit little OCT motion contrast in comparison to MNPs elastically bound to a target within the tissue (such as a targeted cell receptor, or by being internalized into a subcellular compartment). Tissue

elasticity also provides an important restoring force when the  $B$ -field is switched off, returning the tissue to its original state of deformation. This allows for the application of modulated  $B$ -fields to be used to measure several cycles of repeated deformation, improving the signal-to-noise ratio (SNR), analogous to lock-in detection.

Despite the ability to attain arbitrarily large SNR with repeated measurements, there is a fundamental sensitivity limit to MMOCT given by the ratio of the medium to the particle magnetic susceptibility [29]:

$$\rho = -\frac{\chi_{med}}{\chi} \quad (2)$$

which corresponds to an MIO density on the order of  $\rho = 8 \mu\text{g/g}$  for a typical MIO. This is the MIO concentration where the force from the diamagnetic components of the tissue (which push away from the magnet) exactly balance the force on the particles, and there is no net motion. Below this limit, the tissue is actually pushed away from the magnet, which can be seen particularly if the magnetic field being used is too high. In fact, in [29], [30], it has been shown that there is a decreasing effect of MMOCT contrast with increasing magnetic field if the field is above that needed for the MIOs to reach their saturation magnetization. This is somewhat counter-intuitive, and can be understood by the fact that the diamagnetic tissue magnetization (which is negative) continues to grow with  $B$  even after the MIO are saturated, eventually cancelling out the MIO magnetization. In the other extreme, if the  $B$ -field is too low, the MIO motion will be too minute to detect; thus, a sweet spot should be determined depending upon the target MIO concentration for the given application and phase noise of the OCT system; this sweet spot is typically just a little below the saturation field, which for MIOs is  $\sim 0.1$  T.

The most challenging aspect of an MMOCT system is constructing an appropriate magnetic field delivery system. While some researchers have opted for commercially-available pointed-core solenoids which provide an extremely strong  $B$  field gradient at their tip, this requires illuminating the sample from the opposite direction, limiting studies to thin samples. In comparison, open-air designs such as in Fig. 1 permit an arbitrarily thick sample to be assessed, although do require higher currents to compensate for the lack of a solenoid core material, and thus will need to be water-jacketed to dissipate heat. The most expensive component is typically the programmable power supply ( $\sim 100$ – $250$  W), although a unipolar supply can save cost since MNPs will always be pulled in the same direction irrespective of polarity (see Eq. 1).

Tissue mechanics play an important role in determining the MMOCT sensitivity and imaging speed. The displacement is inversely proportional to the tissue elastic modulus, and thus stiffer tissues will provide lower MMOCT contrast. At the same time, tissue viscoelasticity will slow the response time between the application of the force and the resulting displacement, limiting the maximum frequency that the  $B$ -field can be modulated (in practice, typically  $< 100$  Hz). Use of these lower frequencies avoids heating that occurs in techniques such as magnetic hyperthermia, where MIOs are modulated typically at  $> 100$  kHz

to achieve significant heating effects [31]. In sinusoidally modulated MMOCT where the  $B$ -field is modulated several cycles per transverse position, this limits the accessible imaging acquisition time to several seconds. The new generation of high frame rate OCT systems ( $>100$  fps) are currently allowing for MMOCT to be performed by collecting several frames (or volumes [32]) per  $B$ -field cycle, and thus frame rates nearing video rate are now possible.

It should be noted that there are a variety of methods for performing MMOCT that are not necessarily subject to all of the discussion above, such as a two-coil system for MNP contrast in fluids [33], and the use of pulsed, rather than sinusoidal,  $B$ -fields [34]. Also, related platforms for imaging, including optical Doppler tomography, optical coherence elastography (OCE), and optical coherence microscopy (OCM) have been employed with magnetomotive contrast. These will be discussed in more detail in Section V.

### III. PLASMONIC NANOPARTICLE-BASED CONTRAST WITH OCT: THEORY AND PRACTICE

Surface plasmons are a collective excitation of electrons that oscillate across the surface of metals. In nanoparticles, these plasmons are confined to a small area and can become resonantly excited by light, either absorbing or re-emitting the light with high efficiency. In particular, only the noble metals gold and silver exhibit surface plasmon resonances (SPRs) in the visible spectrum, with gold being the only material offering SPRs in the near-infrared (NIR) wavelength regime typically used for OCT.

The fact that gold is a noble metal is also fortuitous for biomedical applications; gold is chemically inert and has been used as a medicine since ancient times [35], although caution should be taken to ensure that the surface charge does not induce cytotoxicity [36].

The SPR property of gold nanoparticles (GNPs) offers a unique opportunity to tailor contrast agents for OCT, as summarized conceptually in Fig. 2. For gold nanospheres, the SPR peak wavelength shifts gradually from  $\sim 535$  to  $635$  nm for particles from  $20$  to  $140$  nm, respectively [37]. To access longer wavelengths, shaped particles such as ellipsoids (or, in practice, nanorods) are used which split the resonance modes along the principle axes of the particle. In the case of gold nanorods, aspect ratios of  $2.4$  to  $5.6$  provide longitudinal SPRs from  $\sim 650$  to  $950$  nm, respectively [38].

In addition to nanorods, GNPs with more complex geometries, like nanocages [39], nanorings [40] and nanoshells [41], also offer largely tunable spectral ranges. This is useful in multi-channel measurements as seen with polarization-sensitive OCT [42] and SOCT [43]. Furthermore, shifting SPRs toward shorter wavelengths tailors the GNPs for use with higher-resolution OCT systems. Conversely, shifting the SPR toward longer wavelengths tailors them for OCT systems with larger penetration depths. This makes GNPs attractive for use with different systems depending upon the application.

A very important consideration is whether the SPR is predominantly light-absorbing or light-scattering in nature. Smaller particles are absorbing, with a transition to scattering-dominance at

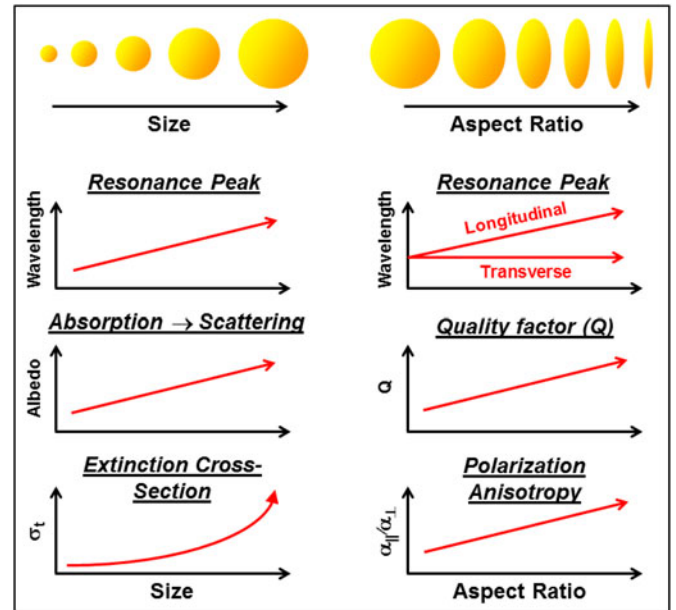


Fig. 2. General trends in the optical properties of gold nanospheres and prolate ellipsoids as a function of size and aspect ratio, respectively. The various contrast methods (SOCT, PTOCT, and DOCT) each have different figures of merit that dictate different particle sizes and shapes.

$\sim 100$  nm in size [44]. Thus, applications such as photothermal OCT (PTOCT), which requires high light absorption to generate heat, will tend to prefer smaller GNPs, while diffusion OCT (DOCT) exploits dynamic light scattering (DLS) and prefers larger GNPs. Spectroscopic OCT (SOCT) can, in theory, be designed to sense either wavelength-dependent absorption or scattering, although in practice tends to employ absorption due to the already high scattering coefficient of tissue. Importantly, the optical extinction coefficient scales with the particle volume,  $V$ , in the absorbing regime, and  $V^2$  in the scattering regime [45], such that increasing particle size can rapidly increase optical detection. However, this must be balanced against the needs for smaller particles that can be effectively delivered to the biological target of interest.

An important consideration for SOCT is the quality factor ( $Q$ ) of the SPR, as higher  $Q$  will provide a stronger wavelength-dependence, as well as the potential for multi-channel detection schemes. The  $Q$  of gold nanorods in particular has been established to be superior to gold spheres [46]. Another property of GNPs is polarization anisotropy, e.g., the ratio of the optical polarizability between light that oscillates parallel and perpendicular to the geometrical axis of the SPR, which can be exploited for DOCT. The need for polarization anisotropy in methods like DOCT, discussed below, also suggests the use of anisotropic particles such as gold nanorods.

There are several notable GNP geometries missing from Fig. 2, including gold nanoshells [41] and nanocages [47], which will be discussed in greater detail in Section VI.

#### A. Spectroscopic Contrast

SOCT was originally developed to assess intrinsic optical properties through analysis of the backscattered OCT spectrum

[48]. When GNPs are added to tissue, they modify the native wavelength-dependent scattering and absorption coefficients ( $\mu_a(\lambda)$  and  $\mu_s(\lambda)$ , respectively). The resulting OCT signal amplitude is proportional to  $\mu_s(\lambda)$  (presumed to scale with the backscattering coefficient,  $\mu_b$ ) and decays exponentially in depth,  $z$ , proportional to the total extinction  $\mu_t = \mu_s + \mu_a$  [49]. Thus, in SOCT, relative  $\mu_s$  can be obtained from the overall OCT signal amplitude, and  $\mu_a$  is subsequently inferred from a differential with respect to  $z$ .

Because tissue is highly scattering in the NIR ( $\mu_a \ll \mu_s$ ) [50], most applications of GNPs with SOCT have employed absorbing GNPs. If we consider the resulting absorption and scattering coefficients in terms of the presence of tissue light scattering structures and absorbing GNPs with densities of  $\rho_s$  and  $\rho_a$ , respectively, we can write:

$$\begin{aligned}\mu_a(\lambda, z) &= \varepsilon_a(\lambda) \rho_a(z) \\ \mu_s(\lambda, z) &= \varepsilon_s(\lambda) \rho_s(z)\end{aligned}\quad (3)$$

where  $\varepsilon_s$  and  $\varepsilon_a$  are the molar extinction coefficients of the tissue and GNPs, respectively. Thus, characterization of  $\varepsilon_s$  and  $\varepsilon_a$  in advance of an imaging experiment can allow for estimation of the density of absorbing GNPs,  $\rho_a$ , quantitatively. A least-squares solution for this problem exists [51], and models accounting for various noise contributions have been described [52]. There are, of course, many other computational methods for detecting wavelength-dependent absorbers within tissues, including simpler centroid-shifting methods [53], and spectral triangulation [54]. The choice of method should balance the need for accuracy and presence of particular sources of noise (such as modulation of wavelength-dependent scattering in the native tissue) against imaging speed.

Building upon this basic concept, more advanced methods for SOCT-based GNP contrast have been developed. For example, differential contrast between OCT images from a non-overlapping dual-band spectrum has been applied for discrimination between GNPs with different SPR wavelengths [55]. In a similar vein, GNPs synthesized with varying SPR wavelengths have been suggested for contrast imaging of multiple targeting moieties simultaneously [56]. Interestingly, while not demonstrated with SOCT, it may be possible to exploit the SPR red-shift that occurs between GNPs as they are brought into close proximity, which allows one to sense an activatable event such as binding of multiple GNPs to a single location on a cell surface [57].

### B. Photothermal Contrast

When absorbing GNPs are used with an SPR in the wavelength band of the OCT light, it is often difficult to avoid photothermal heating. Fortunately, the photothermal effect itself can be exploited for contrast. As heat dissipates from the GNP into the surrounding aqueous tissue, two effects occur simultaneously: the refractive index ( $n_0$ ) decreases with temperature  $T$  according to  $dn/dT$  (which is on the order of  $-10^{-4}/^\circ\text{C}$  for water), while the volume increases according to the volume expansion coefficient,  $\beta$  (which is on the order of  $2 - 4 \times 10^{-4}/^\circ\text{C}$

for water). These terms respectively decrease and increase the optical path length, with the net path length change being given by the following [58]:

$$\Delta z = L_0 \frac{dn}{dT} \Delta T + L_0 \beta n_0 \Delta T + O(\Delta T^2). \quad (4)$$

While these effects this may appear to be small, the cumulative effect of over even  $L_0 = 10 \mu\text{m}$  of path length and a temperature rise of  $1^\circ\text{C}$  can give rise to an optical path length difference on the order of 3 nm, which is within reach of many phase-sensitive OCT systems.

Like MMOCT, PTOCT is a modulated contrast method (dark contrast method), which offers greater SNR than methods requiring prior knowledge or reference images of tissue in the absence of contrast agents [16]. Typically, PTOCT is performed by modulating a heating beam tuned to the GNP SPR but outside the passband of the OCT beam. OCT can then monitor the resulting modulation of  $\Delta z$  and employ lock-in detection. The dynamics of heat dissipation dictate imaging speed in this method; use of a laser intensity that is too high, or modulation without sufficient rest period between heating events results in loss of thermal confinement that can lead to creep of the tissue temperature over several modulation cycles [58]. Because the temporal response occurs over  $\sim 1$  ms, modulation speeds on the order of 10–100 s of Hz are typical [58], [59].

More advanced methods have been employed to enhance the PTOCT signal. Initially demonstrated using OCM [60], photothermal optical lock-in OCT (poli-OCT) decreases PTOCT acquisition time and eliminates the need for post-processing of images using temporal phase data by inducing a phase modulation in the reference arm of the interferometer. Setting the integration time of the camera to an integer multiple of the frequency shift period results in low-pass filtering of the signal, isolating the signal due to photothermal heating and reducing signals from static scatterers to zero [61]. Poli-OCT increases image acquisition rates to allow for capturing *in vivo* time-course dynamics (e.g., blood flow and drug delivery).

### C. Diffusion Contrast

An emerging form of OCT contrast is exploiting the Brownian diffusion of GNPs as a unique, time-dependent signature assessed by DLS techniques. DLS is a technology traditionally used for particle sizing, where the ability to depth-resolve DLS signatures in OCT was noted early in the development of OCT [62]. Today, DLS-based OCT is most commonly used to quantify aspects of hemodynamics by measuring red blood cell diffusion and flow [63]. For the purposes of contrast imaging, DLS of GNPs provides some unique opportunities for assessing viscous liquid properties [64] and porous properties [65] of tissues. This is because the translational diffusion rate,  $D_T$ , of spherical particles within a viscous medium can be described by the Stokes–Einstein relation:

$$D_T = \frac{k_B T}{6\pi\eta a} \quad (5)$$

where  $\eta$  is the medium viscosity,  $a$  is the particle radius, and  $k_B$  is the Boltzmann constant. In practice, the diffusion rate can be quantified by computing the temporal autocorrelation,  $\Gamma$ , of the OCT signal:

$$\Gamma(\tau) \propto \exp(-q^2 D_T \tau) \quad (6)$$

where  $q$  is the scattering vector equal to  $2k$  in the backscattering geometry of OCT. Importantly, because GNPs are plasmon-resonant, they provide orders-of-magnitude larger optical scattering than non-resonant tissue structures of the same size. Because of the strong size-scaling of optical scattering, tissue features that are larger (on the order of  $\lambda$ ) will dominate the endogenous OCT signal. According to Eq. (5), these larger features will exhibit smaller  $D_T$ , and thus the detection of unusually high  $D_T$  is a unique signature of GNPs within tissue.

The choice of GNPs is therefore dictated by a need for sufficiently large size to provide optical scattering, balanced against the diffusivity of GNPs into the tissue. In practice, gold nanorods of  $\sim 20 \text{ nm} \times 60 - 80 \text{ nm}$  have been found to rapidly homogenize throughout model tissue structures, while being sufficiently large for DOCT detection [65]. Interestingly, gold nanorods also provide polarization anisotropy (see Fig. 2), which provides the ability to measure both rotational ( $D_R$ ) and translational ( $D_T$ ) diffusion for further tissue discrimination [64].

The applications of GNP-based DOCT are growing. In tissues, non-adherent GNPs can be designed to diffuse through extracellular pores to monitor tissue remodeling processes [65] that may provide new insight into cancer growth. In liquids such as mucus, GNPs can provide relative measures of hydration [65], providing a metric for assessing respiratory diseases like cystic fibrosis. More comprehensive details are provided in Section VI.

#### IV. EXPERIMENTAL SYSTEMS OVERVIEW

Table I provides an overview of many (but not all) magnetic- and plasmonic-based OCT contrast systems reported to date, with emphasis on *in vivo* experiments, novel particle geometries, and novel imaging schemes. Within each imaging modality (and within each subset of GNP shape), particles are sorted by size from small to large. When possible, a particle concentration is given to aid in general comparison between the techniques, although the reader should be cautioned that direct comparison of concentrations is not always possible due to varying applications and experimental details.

#### V. MAGNETOMOTIVE OCT EXPERIMENTS

This section is organized as follows. First, the various types of MMOCT systems are described, including phase- versus amplitude-sensitive and sinusoidal versus pulsed systems. Next, types of magnetic particles that have been reported to be used with MMOCT imaging are discussed. Finally, the breadth of potential clinical applications for MMOCT is addressed. While this review is intended to represent the widest variety of ongoing efforts in this field, for the sake of brevity only a subset of publications are able to be addressed.

#### A. System Types

MMOCT was first reported by Oldenburg *et al.* in 2004 [66], with follow-up papers in 2005 [67], [68]. These were obtained using a time-domain OCT system where the  $B$ -field was modulated for each A-scan; thus, scan times were quite long (1 min). Because MMOCT operates by both optical and mechanical principles, tissue phantoms were prepared to mimic the optical and mechanical properties of soft tissue by embedding optically-scattering  $\text{TiO}_2$  particles into a silicone matrix. The addition of varying amounts of MIOs into each phantom allowed for determination of the MMOCT system sensitivity, which was found to be  $220 \mu\text{g}/\text{mL}$ , establishing a starting point for further improvements [68]. The first *in vivo* MMOCT was obtained in African frog tadpoles (*Xenopus laevis*) under anesthesia. Magnetic particles were consumed by tadpoles via their suction feeders and subsequently observed within their digestive tract [68].

This early work was performed using a time-domain OCT system that was not phase-sensitive, and thus contrast was limited to differences in the OCT signal amplitude. To overcome this limitation, a differential-phase OCT system was developed for sensitive displacement measurement [69], which was applied to magnetomotive imaging [70]. Results demonstrated nanoscale resolution of magnetic particle motion within *ex vivo* tissues, where the particles had accumulated within the *in vivo* animal models to demonstrate deliverability [70], [71].

The emergence of spectral- or Fourier-domain OCT provided improved imaging times [72], [73] as well as phase-sensitivity due to the avoidance of moving parts [22]. Crecea *et al.* investigated the spectral-domain amplitude and phase signals from magnetomotion in phantoms, and observed free oscillations induced after application of a step-like  $B$ -field [74]. Further work with phase-resolved MMOCT by Oldenburg *et al.* demonstrated sensitivity to nanomolar concentrations of magnetic nanoparticles under sinusoidal modulation [29]; achieving nanomolar sensitivity marked an important milestone for cell-receptor targeted imaging applications.

The application of pulsed magnetic fields has also been explored for MMOCT. By pulsing the electromagnet, one can reduce coil heating effects endemic to the higher duty-cycle sinusoidal method [34]. Using this technique, phantoms with magnetically-labeled cells at a relatively large standoff distance of 30 mm from the coil were imaged [34], and labeled cells within three-dimensional (3-D) constructs have also been contrasted in pulsed MMOCT [75].

While MMOCT is traditionally used to image elastically-bound MIOs within tissue, the ability to contrast unbound MIOs in free solution, such as the blood volume, would provide new translational opportunities. To address this need, Kim *et al.* developed the dual-coil MMOCT system displayed in Fig. 3 [33]. In this configuration, the coils are used to apply opposing forces in sequence, in order to initially displace then restore MIOs in solution. Thus, it avoids the need for an intrinsic elastic restoring force to generate a modulated displacement signal.

Magnetomotive optical coherence elastography (MMOCE) is a natural extension of MMOCT that exploits the dependence of induced tissue vibration on its intrinsic mechanical properties.

## OVERVIEW OF MAGNETIC AND PLASMONIC OCT EXPERIMENTS

	Citation	Type of particle <sup>#</sup>	Particle coating	Size (nm) <sup>##</sup>	Concentration <sup>###</sup>	Type of sample	Application		
Magnetic Nanoparticles	OCT	Oh, 2008 <sup>[64]</sup>	MIO, bead	Dextran	5 (core), 40 (OD)	0.2 mM Fe/kg	<i>ex vivo</i> rabbit tissue	atherosclerosis	
		Oldenburg, 2010 <sup>[74]</sup>	Feridex <sup>TM</sup> , cluster	Dextran	5 (core)**, 36-100 (OD)	70 µg/mL	<i>ex vivo</i> porcine artery	thrombosis	
		Oldenburg, 2012 <sup>[75]</sup>	MIO, bead	Dextran	10-20 (core), 20-30 (OD)	41-43 µg/mL	<i>ex vivo</i> blood clots	thrombosis	
		Oh, 2007 <sup>[63]</sup>	Feridex <sup>TM</sup> , cluster	Dextran	5 (core)**, 36-100 (OD)	1.5 mM Fe/kg	<i>ex vivo</i> liver, spleen	macrophages	
		Oldenburg, 2005 <sup>[4]</sup>	Fe <sub>3</sub> O <sub>4</sub> , bead	(none)	20-30 (core)	NA	<i>in vivo</i> tadpole	optical biopsy	
		John, 2010 <sup>[79]</sup>	MIO, bead	Antibody, dextran	20-30 (core)	NA	<i>in vivo</i> rat tumor	breast cancer	
		Oldenburg, 2008 <sup>[81]</sup>	Fe <sub>3</sub> O <sub>4</sub> , bead	(none)	20-30 (core)	2 nM*	phantom	<i>ex vivo</i> rat tumor	tumor imaging
			MIO, sphere	COOH	20 (core), 22 (OD)	NA			
		John, 2012 <sup>[82]</sup>	Ferrofluid/dye-filled protein sphere	Peptide	20-30 (core)**, 2000-5000 (OD)	1 × 10 <sup>11</sup> /mL	<i>ex vivo</i> rat tumor	cancer	
		Kim, 2013 <sup>[30]</sup>	Ferrofluid/dye-filled protein sphere	Peptide	20-30 (core)**, 2000-5000 (OD)	.001pM	liquid phantom	intravascular	
		Wang, 2010 <sup>[88]</sup>	MIO, bead	Streptavidin	1000 (core)	<4 mg/mL	<i>in vivo</i> mouse eye	anterior eye	
							<i>in vitro</i> mouse eye		
		Kim, 2014 <sup>[83]</sup>	Ferrofluid/dye-filled protein sphere	Peptide	20-30 (core)**, 2000-5000 (OD)	4.48 pM	<i>ex vivo</i> porcine artery	atherosclerosis	
		Huang, 2015 <sup>[25]</sup>	Fe <sub>3</sub> O <sub>4</sub> , cluster	NA	NA	<150 ppm	cell culture	cancer	
		Oldenburg, 2005 <sup>[60]</sup>	Fe <sub>3</sub> O <sub>4</sub> , powder	(none)	1920 (core)	<1.2 mg/mL	cell culture	cell labeling	
Crecea, 2009	Fe <sub>3</sub> O <sub>4</sub> , bead	(none)	25 (core)	2.5 mg/mL	phantom	rheology			
					<i>ex vivo</i> rabbit tissue				
					phantom				
Crecea, 2013 <sup>[70]</sup>	Fe <sub>3</sub> O <sub>4</sub> , bead	(none)	25 (core)	NA	<i>ex vivo</i> rabbit tissue	microrheology			
					phantom				
Ahmad, 2014 <sup>[29]</sup>	Fe <sub>3</sub> O <sub>4</sub> , bead	(none)	50-100 (core)	250 mg/mL	phantom	elastography			
					<250 mg/mL				
					<250 mg/mL				
Crecea, 2014 <sup>[71]</sup>	Ferrofluid-filled protein sphere	NA	900-3500 (OD)	NA	3D mammary cell culture	cellular mechanics			
							MIO, bead	PS & dye	1000-2000 (OD)
Kim, 2007	Feridex <sup>TM</sup>	Dextran	5 (core)**, 36-100 (OD)	360 µg Fe / mL*	capillary tube	fluid flow			
Plasmonic Nanoparticles	DOCT	Lee, 2011	Gold, ring	PEG	179 (OD), 149 (ID), 97(h)	<40 pM	<i>ex vivo</i> mouse liver	drug delivery	
		Chhetri, 2011 <sup>[57]</sup>	Gold, rod	CTAB	53 (L), 15 (d)	1320 pM	viscous fluids	viscometry	
		Chhetri, 2014 <sup>[58]</sup>	Gold, rod	PEG	83 (L), 22 (d)	112 pM*	3D airway & breast culture	tissue nanotopology	
		Oldenburg, 2013 <sup>[124]</sup>	Gold, rod	PEG	83 (L), 22 (d)	<547 pM	3D tumor organoids	molecular imaging	
	PTOCT	Chi, 2014 <sup>[119]</sup>	Gold, ring	NA	155 (OD), 130 (ID), 50 (h)	<3.32 pM	<i>ex vivo</i> pig liver	molecular imaging	
		Tucker, 2015 <sup>[54]</sup>	Gold, rod	PEG	45.2 (L), 13.2 (d)	<200 pM	<i>in vivo</i> mouse ear	molecular imaging	
		Xiao, 2013 <sup>[118]</sup>	Gold, smart rose	C <sub>5</sub> H <sub>7</sub> NO <sub>3</sub>	10 (d)**	<60 nM	cell culture	cancer	
							phantom		
		Paranjape, 2010 <sup>[117]</sup>	Gold, rose	dextran	~30 (d)	0.531 pM*	phantom	macrophages	
							<i>ex vivo</i> aorta		
		Adler, 2008 <sup>[51]</sup>	Gold, shell	NA	136 (OD), 120 (ID)	<16.6 pM	GNP solution	molecular imaging	
		Nahas, 2014 <sup>[120]</sup>	Gold, shell	PEG	150 (OD), 130 (ID)	<4.15 pM	<i>ex vivo</i> mouse skin	phototherapy	
		Zhou, 2010 <sup>[116]</sup>	Gold, shell	NA	152 (OD), 120 (ID)	<8.30 pM	<i>ex vivo</i> breast tissue	molecular imaging	
		Skala, 2008 <sup>[52]</sup>	Gold, sphere	PEG	60 (d)	26 pM*	liquid phantom	molecular imaging	
							<39 pM		cell culture
Cang, 2005 <sup>[40]</sup>	Gold, cage	NA	35 (L,w,h)	<500 pM	phantom	molecular imaging			
Wei, 2009 <sup>[97]</sup>	Gold, rod	CTAB	NA	2 pM	phantom	molecular imaging			
Oldenburg, 2009 <sup>[114]</sup>	Gold, rod	CTAB	45 (L), 15 (d)	<10-20 nM	<i>ex vivo</i> breast tissue	breast cancer			
Jia, 2015 <sup>[98]</sup>	Gold, rod	PEG-Tat	50-59 (L), 10 (d)	<83 pM	cell culture	retina			
Rawashdeh, 2015 <sup>[115]</sup>	Gold, rod	CTAB	75 (L), 20 (d)	<912 nM	<i>ex vivo</i> chicken	blood vessels			

<sup>#</sup>magnetic iron oxide (MIO).

<sup>##</sup>indicated by core, outer diameter (OD) inner diameter (ID), length (L), width (w), diameter (d), or height (h).

<sup>###</sup>by mass density (w/v); particle density (v<sup>-1</sup>), particle molarity (pM-nM), or dose (molarity Fe/w).

\* minimum concentration needed for detection.

\*\* particle size within cluster or fluid.

While the vibrational response of tissues to external loading forces was demonstrated via OCE [76], the ability to use MIOs to apply those forces internally in tissues offers added flexibility and with lower strain rates to avoid nonlinearities. In 2013, Crecea *et al.* demonstrated MMOCE by studying free oscillations of *ex vivo* tissues in response to stepped forces, where the vibrational frequency and rise time were proportionally and

inversely related to the elasticity, respectively [77]. Then, in 2014, Crecea *et al.* adapted these methods on an OCM setup to investigate biomechanical properties on the single-cell scale [78]. Other efforts in MMOCE have investigated shear-wave methods commonly used in OCE [79].

The frequency-dependence of tissue mechanical properties can also be exploited by interrogating MIOs in tissues at varying

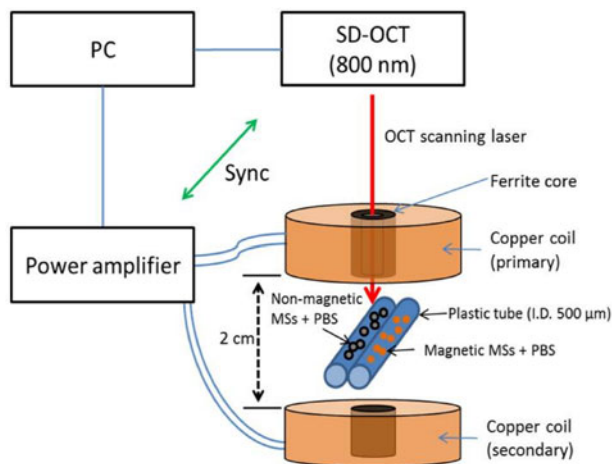


Fig. 3. Schematic and output of a dual-coil magnetomotive OCT setup employing magnetically labeled microspheres in a flow phantom containing phosphate-buffered saline. (Reprinted with permission from [33]).

frequencies. In 2015, Ahmad *et al.* demonstrate this principle in phantoms and tissues, with validation against finite-element modeling [80]. As an extension of this, Oldenburg and Boppart developed a resonant acoustic spectroscopy method to measure elasticity of small biosamples with high precision [81]. Interestingly, this has found particular application in the assessment of blood clot elasticity [82], [83], which may in future work connect with the same group's efforts in magnetically-loaded platelet labeling of blood clots [30].

### B. MIO Particle Sizes and Types

Here we will cover the general classes of MIOs used in MMOCT; for more detailed information, the reader is directed to a review on this topic [84]. The choice of MIO particle core size and coating for MMOCT should take into consideration the desired magnetic properties and targeting moieties. For nanoparticles (<100 nm), several general classes of MIOs have been used. One of the most common are dextran-coated MIOs produced by a precipitation method that can be performed without special equipment [85]. These tend to produce particles in the 10–20 nm size range, while the dextran coating can increase their hydrodynamic diameter to 30 nm or more, and have successfully been used in several MMOCT studies [82], [86]. An important class of dextran-coated MIOs are MRI contrast agents FDA-approved as liver contrast agents; of these, Feridex IV<sup>TM</sup> has been used in several MMOCT studies [30], [70], noting that they are comprised of clusters of ~5 nm MIO cores embedded in a larger dextran matrix, with an overall average hydrodynamic diameter of 36 nm [23].

To generate nanosized MIOs that have greater size monodispersity, synthesis can be accomplished by the thermolysis of iron precursors [87]. Commercially available particles prepared in this way are available with a variety of coatings (Ocean Nanotech, Inc.); for MMOCT, COOH-coated MIOs have been employed with success [81], [88].

The conjugation of antibodies onto MIOs confers them with specificity for specific over-expressed cell receptors. John

*et al.* conjugated anti-HER2 onto dextran-coated MIO particles, demonstrating specific uptake into tumors via MMOCT in an *in vivo* rodent model of breast cancer; the same particles provided MRI contrast for validation of the particle localization within tumors [86].

At the same time, conjugation of fluorescent dyes confers multi-functional (OCT-fluorescence) imaging capabilities that can aid in validating the biodistribution of MIOs used in animal models *in vivo*. In particular, oil-filled albumin microspheres offer a platform particularly amenable to multi-functionalization. Several studies have demonstrated a class of such microspheres that are filled with an oil-based ferrofluid containing fluorescent dye, while being surface labeled with a peptide to target sites of cancer and atherosclerosis [89], [90]. Because these protein microspheres are nominally 2–5  $\mu\text{m}$  in size, they are appropriate for vascular targets such as atherosclerosis, as well as cancers exhibiting “leaky vasculature” where blood pool agents will tend to accumulate [91]. In addition to these customized multifunctional particles, MMOCT has also been used with commercially available magnetic microbeads that offer fluorescent as well as surface conjugation capabilities [78].

### C. Contrast Imaging Applications

While MMOCT is currently a pre-clinical technology, the breadth of research studies implicates a wide variety of future clinical applications. One class of applications lies in tracking magnetically-labeled cells, the feasibility of which was initially demonstrated in 3-D cell culture in early MMOCT work [67]. Because macrophages readily phagocytose nanoparticles, MMOCT can be used to track the fate of macrophages in the liver and spleen [70], or macrophage-laden sites of vulnerable atherosclerotic plaques [71]. Also, the ability to track stem cells is highly sought after for monitoring stem cell therapies; recently, Cimalla *et al.* demonstrated MMOCT of labeled stem cells *in vitro* [75], working toward a method for monitoring retinal regeneration.

Blood platelets are a powerful tool for functional imaging, as they readily take up foreign particles via a mechanisms known as “covercytosis” [92], and play a crucial role in hemostasis and thrombosis [93]. Thus, the highly functional nature of platelets can be used to target sites of vascular damage where blood clots form. As shown in Fig. 4, MMOCT of magnetically-labeled platelets flowed through *ex vivo* porcine arteries exhibits highly specific contrast only to damaged blood vessel walls [30]. In combination with existing technologies for cardiovascular imaging [4], MMOCT of labeled platelets, macrophages, or functionalized microspheres discussed in the previous subsection, may play a role in identifying sites of vulnerable atherosclerotic plaque.

Moving beyond pure imaging applications, there has been recent development in the area of theranostics (i.e., simultaneous diagnostics and treatment). Huang *et al.* report a novel clustered magnetic nanoparticle with both light scattering properties at 860 nm for OCT imaging, and absorbing properties at 1064 nm for photothermal therapy [27]. Thus, cancer cells were shown to be both imaged and subjected to hyperthermia by the same

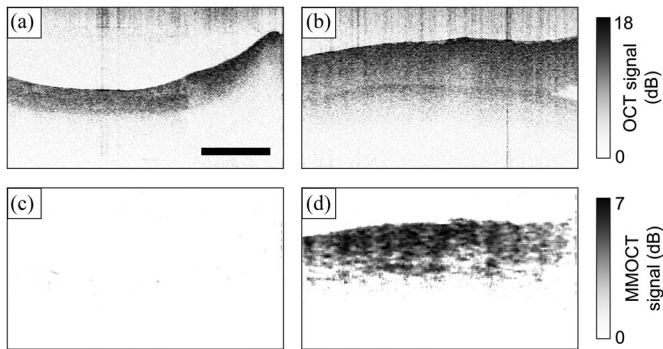


Fig. 4. Sample B-mode images of *ex vivo* porcine arteries following exposure in a flow chamber to SPIO-RL platelets. (a) OCT image of control artery (b) OCT image of damaged artery (c) magnetomotive OCT image of control artery (d) magnetomotive OCT image of damaged artery. Note that each artery is longitudinally cut with the luminal wall facing upward. Scale bar: 0.5 mm (Reprinted with permission from [30]).

particles. Interestingly, the potential exists to provide heating to tissue directly via magnetic fluid hyperthermia by applying a magnetic field modulated in the 100's of kHz [94], a technique that has yet to be explored in conjunction with MMOCT.

Given the widespread use of OCT in ophthalmic applications, it should be noted that MMOCT has also been explored in this area. In 2010, Wang *et al.* reported the ability to contrast magnetic beads in the anterior segment of a mouse eye, which was overlaid on the structural OCT image [95]. The same group subsequently developed a SOCT-MMOCT platform for detecting cochlin (a precursor of glaucoma) in the trabecular meshwork of mice using anti-cochlin labeled magnetic particles [96].

Elastographic applications of magnetomotive imaging via MMOCE are also under development. For example, measurements of lung epithelium compliance can aid in tracking the progression of bronchiectasis in diseases such as COPD; Chhetri *et al.* demonstrated MMOCE measurements of *in vitro* human tracheo-bronchial-epithelial cells [97]. More recent technological developments by Ahmad *et al.* have demonstrated promising capabilities for shear-wave based MMOCE in tissues *ex vivo* [79].

All of these potential applications will be aided by the continually improving acquisition rates in OCT technology, which have recently been shown to enable acquisition of entire OCT volumes during modulation of the magnetic field for volumetric MMOCT [32].

## VI. PLASMONIC NANOPARTICLE OCT EXPERIMENTS

Nanoparticles have recently gained popularity for medical imaging and therapeutics due to their size and unique optical properties. The size and shape of these nanoparticles govern their optical response with the wavelength at plasmon resonance ( $\lambda_{SPR}$ ) typically occurring in the NIR “biological imaging window.” By altering the size and shape of these plasmonic GNPs,  $\lambda_{SPR}$  can be shifted to wavelengths from red into the NIR, within the detection range of typical OCT systems, making them attractive candidates as contrast agents in tissue using current OCT imaging techniques.

The GNPs reviewed here are primarily gold taking the shape of rods, roses, spheres, shells, cages, and stars/branches. These shapes offer their own unique optical properties and biological characteristics to be discussed. Nanospheres offer a plasmon resonance mode with dependence on diameter [98]; cylindrically-shaped nanorods offer two plasmon resonant modes (longitudinal and transverse) that can be tuned to the near-IR by adjusting the aspect ratio of their length ( $L$ ) to diameter ( $d$ ), [99], as described in Section III. Nanoroses are a conglomeration of smaller nanospheres ( $\sim 10$  nm), that alone, are too small to exhibit a plasmon resonance, but do as a whole [100]. Nanostars are created from spherical gold seeds and have gold branches stemming from the center. The plasmon resonance of these structures is governed by the length of these branches and the size of the initial seed, that acts to enhance plasmon resonance at the tips [101]. Gold nanocages, created from silver nanostructures through a galvanic replacement process, are gold frames taking various geometric shapes (e.g., cubes and polyhedrons). The  $\lambda_{SPR}$  of these structures, tunable to the NIR at exceptionally small sizes, are governed by the outer width ( $w$ ) and frame thickness ( $t$ ), with absorption dominating for structures  $< 45$  nm [39]. Nanoshells, created by growing gold on a dielectric core, can be tuned with higher precision than other GNPs by altering the fabrication materials and size (outer diameter, OD, and inner diameter, ID), [41]. Finally, nanorings exhibit a plasmon resonance dependent upon the ratio of the outer diameter to the ring thickness. Nanorings can exhibit redshifts into the NIR as large as 100's of nm by making small changes to the ring thickness, while keeping the overall outer diameter constant [40].

The properties of these GNPs offer unique contributions that lend to a wide variety of biomedical imaging, diagnostic, and therapeutic applications. Below, we review this variety of applications using SOCT, PTOCT, and DOCT.

### A. Spectroscopic Systems

In SOCT, localized spectral measurements are taken within the OCT image. However, the strongly modulated spectrum of tissue light scattering, and the fundamental trade-off between spatial and spectral resolution makes SOCT challenging for biomedical applications. Several techniques have been described to overcome these challenges, including differential absorption [102], spectral fractionation [103], and spectral triangulation [104]. These methods require scatterers with known spectral characteristics that can be tuned with respect to the OCT signal bandwidth ( $\Delta\lambda_{OCT}$ ), for which GNPs are well suited. Before discussing the application of GNPs for spectroscopic (wavelength-dependent) contrast, it is prudent to first mention work done to enhance intensity-based contrast (i.e., changes to the overall OCT signal intensity) through exploitation of GNP's unique absorption and scattering characteristics.

Because GNPs strongly absorb/scatter light at tunable wavelengths, OCT intensity imaging can be enhanced for better contrast and penetration in tissue. Oldenburg *et al.* first described gold nanorods as contrast agents in OCT using their low backscattering albedo compared to that of tissue [44].

Around the same time, Chen *et al.* investigated small nanocages (<40 nm) as absorptive contrast agents in OCT, with implications for cell targeting in both diagnostics and therapeutics. These studies paved the way for contrast enhancement using highly absorbing/scattering GNPs. For example, nanoshells have been used in imaging and ablating tumors in mice [105] and contrasting *in vivo* on pig skin [106] and rabbit skin [107]; nanorods have been used to enhance contrast in tumors [108] and *in vivo* mouse eyes [109]; nanostars have been used in cell imaging [110]; and nanoparticle accumulation in tumors has been monitored [111].

Building upon these works, investigators have derived new methods and applications of OCT intensity contrast. For example, Tseng *et al.* showed that strong absorption by gold nanorings at  $\lambda_{OCT}$  could heat pig adipose tissue during imaging, changing the tissue properties and thereby enhancing contrast [112]. Xi *et al.* introduced a new method of characterizing nanoparticle properties by cross-referencing with tissue void of nanoparticles [113]. Doppler OCT has been enhanced using gold nanorods by Wang *et al.* for imaging ocular flow [114]. Sirotkina *et al.* found that OCT intensity enhancement could be used to estimate GNP accumulation in tumors for guided laser hyperthermia [115]. Later, Coughlin *et al.* showed that by conjugating gold nanoshells with Gadolinium, contrast could be enhanced for MRI and X-Ray, in addition to OCT, for multimodal diagnostics and therapeutics in cancer [116]. Lastly, the growth of nanocubes has been studied by Ponce de Leon *et al.*, by monitoring enhanced contrast during the nanocube growth [117].

While extensive work has been done studying intensity contrast enhancements using GNPs, few have exploited their wavelength-dependent properties to provide more specific contrast against the tissue background. Cang *et al.* introduced gold nanocages as contrast agents in SOCT [47]. The strong absorption at  $\lambda_{SPR}$  for the 35 nm cages allowed for stronger contrast within  $\Delta\lambda_{OCT}$ , providing contrast via both the spectral content and change in overall OCT intensity (shown in Fig. 5). Oldenburg *et al.* extended this technique, first into interlipid phantoms [118], and then into *ex vivo* tissue using gold nanorods [119]. The authors showed that relative nanorod density was evident against strong scattering in human carcinoma breast tissue, lending toward an *in vivo* human tumor contrast agent.

Other methods of SOCT have recently been employed. Wei *et al.* demonstrated the use of GNRs with different aspect ratios, thus different  $\lambda_{SPR}$ , as a method of differential absorption OCT, with implications in molecular imaging and contrasting highly scattering tissues [102]. Expanding on differential absorption contrast techniques, Rawashdeh *et al.* showed that a dual-bandwidth OCT system was capable of providing spectroscopic contrast using different sizes of nanorods tuned to different  $\lambda_{SPR}$  [43]. This technique was demonstrated in agar/TiO<sub>2</sub> phantoms and *ex vivo* muscle tissue. Similarly, Jia *et al.* employ a new method of spectral fractionalization by dividing the OCT bandwidth into sub-bands, providing OCT contrast by comparing the ratio of short to long wavelengths [103]. They demonstrate this method in an interlipid tissue phantom and *in vitro* using a 3-D cell culture, moving toward imaging the human retina *in vivo*.

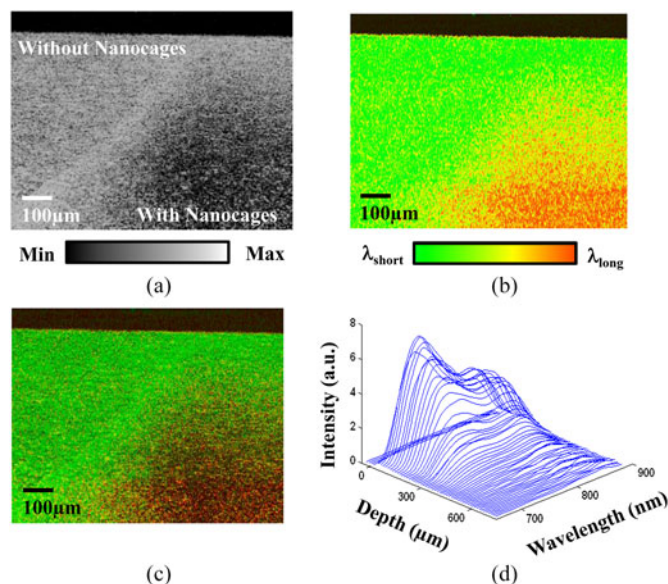


Fig. 5. Spectroscopic OCT images of TiO<sub>2</sub> gelatin phantom, with right side doped with 35 nm nanocages. (a) Standard OCT showing decreasing signal in location with absorbing nanocages. (b) Spectroscopic OCT showing changes in scattered spectra. (c) Hue-Saturation-Value image of the same cross section with hue representing centroid wavelength, and saturation/value representing OCT intensity. (d) Plot of intensity versus depth versus wavelength. (Reprinted with permission from [47]).

## B. Photothermal

PTOCT provides enhanced tissue contrast by exploiting the photothermal properties of GNPs heated at  $\lambda_{SPR}$ . This method is especially attractive for cancer applications due to its ability to both detect GNPs in tissue and induce a therapeutic response by tissue through GNP heating. The following describes work that has been done using GNP contrast enhancement with PTOCT.

This was first demonstrated nearly simultaneously by two research groups. Adler *et al.* introduced 120 nm gold nanoshells for contrast enhancement using PTOCT, demonstrated in tissue phantoms [58]. Skala *et al.* applied PTOCT in two-dimensional (2-D) and 3-D cell cultures using 60 nm gold nanospheres [59]. Zhou *et al.* demonstrated the use of nanoshells in *ex vivo* breast tissue, and showed that oversampling improves SNR [120]. More complex nanoparticle constructs were introduced by Paranjape *et al.*, who used gold nanoroses to detect macrophages [121]. Small nanospheres were clustered together, forming roses, to exhibit strong absorption at the tuned  $\lambda_{SPR}$ , making them attractive candidates for PTOCT. The tunability of these clusters post-manufacturing gives them the unique ability to sense different types of environments. These “smart” particles can be engineered to cluster under specific conditions, such that  $\lambda_{SPR}$  shifts into the photothermal imaging window at discrete clustering states. Xiao *et al.* demonstrated this using pH-activated aggregation for cell imaging [122]. Chi *et al.* took advantage of the ability for nanorings to be tuned far into the infrared by using two OCT systems, one with  $\lambda_{OCT}$  matching  $\lambda_{SPR}$ , and the other with  $\lambda_{OCT}$  outside the peak of  $\lambda_{SPR}$  [123]. The authors found that PTOCT could disambiguate the source of scattering seen in conventional OCT images. Furthermore, they

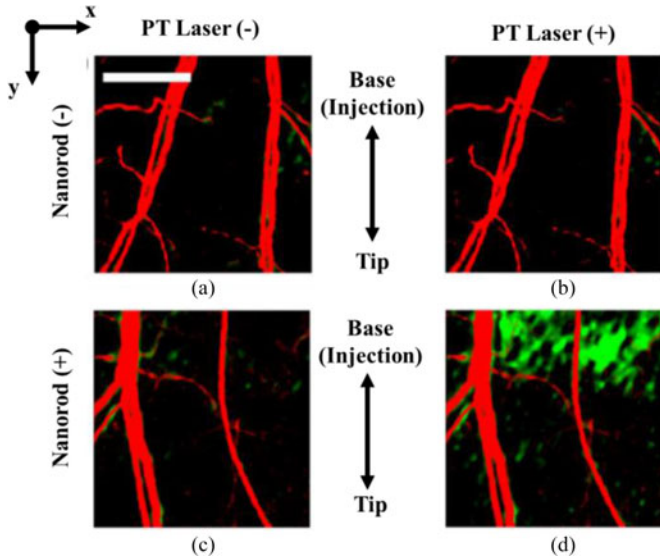


Fig. 6. Matrigel containing gold nanorods injected into an *in vivo* mouse ear showing blood flow via speckle variance (red) and nanorods via PTOCT (green). (a) Blood flow without nanorods and with modulating laser off. (b) Blood flow without nanorods and with modulating laser on. (c) Blood flow with nanorods and the modulating laser off. (d) Blood flow with nanorods and the modulating laser on. (Reprinted with permission from [61]).

found that when using PTOCT with  $\lambda_{OCT} = \lambda_{SPR}$ , only tissue scattering was seen with OCT, with nanorings being detected with PTOCT.

Recently, new techniques have been employed to enhance PTOCT abilities using GNPs. Nahas *et al.* combined full-field OCT (FFOCT), which collects high resolution ( $\sim 1 \mu\text{m}$ ) *en face* 2-D images, with PTOCT techniques using nanospheres [124]. Because FFOCT only images the surface of the tissue, thermal responses of the tissue to modulated energy pulses were delayed with rates dependent upon particle depth. The authors were able to extract the depth location of nanospheres in tissue based on these response delay times to triangulate the location of nanospheres in 3-D tissue. This technique allows the combined benefit of high resolution FFOCT and cell targeting with PTOCT. In addition to resolution enhancement, speed of PTOCT has been improved using optical lock-in techniques (coined poli-OCT), previously described by Pache *et al.* for OCM [60]. Tucker-Schwartz *et al.* employed these methods to improve imaging speed in an *in vivo* mouse ear [61]. Here, they show that poli-OCT can disambiguate motion due to blood flow against the PTOCT signal (see Fig. 6).

### C. Diffusion

As technology progresses with OCT, new methods are possible owing to increased imaging rates and resolution. Particles exhibit a natural Brownian motion that can be measured using DLS within a coherence volume [62]. The rapid collection rates and coherence gating techniques used in spectral-domain OCT (SD-OCT) makes it an attractive candidate for measuring these movements using DLS, as has previously been shown [125]. Furthermore, SD-OCT with polarization sensitivity (PS-OCT)

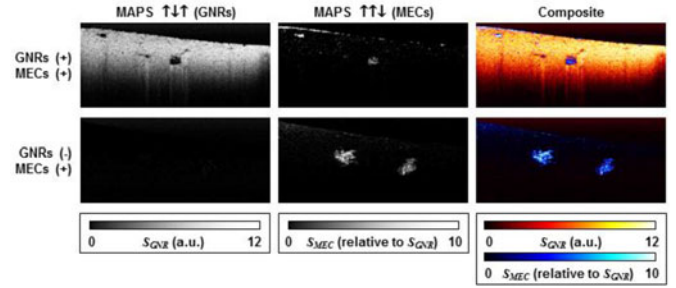


Fig. 7. MAPS signature in a cell culture containing mammary epithelial cells where DOCT was used to enhance contrast of tissue containing gold nanorods against cells void of nanorods. (Reprinted with permission from [42]).

allows for discrimination between optically anisotropic scatterers (like nanorods) and isotropic particles (like cells). The small size and strong scattering of GNPs make them excellent candidates for DOCT.

Diffusion of gold nanorings was first tracked by Lee *et al.* The authors were able to contrast diffusion of these nanorings against native tissue by mapping OCT speckle variance within the image to track the diffusion of these particles over time [126]. Exploiting the optical anisotropy of nanorods, Mehta and Chen used simulations to show enhanced polarization sensitive contrast using a chiral nanostructure constructed from two nanorods [127]. Chhetri *et al.* used this polarization sensitivity to monitor rotational motion of rods, which gives rise to polarization dependent intensity fluctuations. Using DLS theory, the authors showed the rotational diffusion of gold nanorods could accurately predict the viscosity of diffusion in Newtonian liquids [64]. Oldenburg *et al.* then used DOCT to discriminate between tissue and cells using the decorrelation time of speckle fluctuations ( $A$ ) in addition to the cross-polarized intensity signals (PS) that are only evident from nanorod scatters [42]. The authors found that these properties, along with cellular motility measurements ( $M$ ), created unique MAPS signatures by which cells and tissue could be clearly contrasted, with applications ranging from functional drug delivery to quantification of tissue properties. Fig. 7 shows an example of this MAPS (motility-amplitude-polarization-sensitive) signature in artificial tissue seeded with mammary epithelial cells. This group later extended DOCT measurements to quantify non-Newtonian fluids (polyethylene glycol) which led to quantification of polymeric tissues like mucus and collagen. Chhetri *et al.* showed that nanorod diffusion could predict the diseased state of mucus, with implications in treating respiratory diseases like Cystic Fibrosis, and the extracellular matrix, with implications for monitoring the diseased state of tissue during tumorigenesis [65].

## VII. CONCLUSION

The use of MIO and plasmonic GNPs offer many advantages for OCT contrast, in addition to excellent biocompatibility. The choice of a particular particle and contrast method should be considered relative to the needed application, ranging from molecular contrast imaging of cell surface receptors, to the quantification of extracellular nanoporosity. All of the above

methods offer sufficiently high imaging speeds and safety to be used *in vivo*, which may lead to new clinical applications for diagnostics, guidance, and treatment monitoring.

## REFERENCES

- [1] D. Huang *et al.*, "Optical coherence tomography," *Science*, vol. 254, pp. 1178–1181, Nov. 1991.
- [2] E. A. Swanson *et al.*, "In vivo retinal imaging by optical coherence tomography," *Opt. Lett.*, vol. 18, pp. 1864–1866, 1993.
- [3] J. A. Izatt *et al.*, "Micrometer-scale resolution imaging of the anterior eye in vivo with optical coherence tomography," *Archives Ophthalmol.*, vol. 112, pp. 1584–1589, 1994.
- [4] I.-K. Jang *et al.*, "Visualization of coronary atherosclerotic plaques in patients using optical coherence tomography: Comparison with intravascular ultrasound," *J. Amer. College Cardiol.*, vol. 39, pp. 604–609, 2002.
- [5] S. A. Boppart, W. Luo, D. L. Marks, and K. W. Singletary, "Optical coherence tomography: Feasibility for basic research and image-guided surgery of breast cancer," *Breast Cancer Res. Treatment*, vol. 84, pp. 85–97, Mar. 2004.
- [6] B. E. Bouma, G. J. Tearney, C. C. Compton, and N. S. Nishioka, "High-resolution imaging of the human esophagus and stomach in vivo using optical coherence tomography," *Gastrointestinal Endoscopy*, vol. 51, pp. 467–474, 2000.
- [7] M. V. Sivak *et al.*, "High-resolution endoscopic imaging of the GI tract using optical coherence tomography," *Gastrointestinal Endoscopy*, vol. 51, pp. 474–479, 2000.
- [8] J. Armstrong *et al.*, "In vivo size and shape measurement of the human upper airway using endoscopic long-range optical coherence tomography," *Opt. Express*, vol. 11, pp. 1817–26, Jul. 2003.
- [9] A. F. Fercher, W. Drexler, C. K. Hitzenberger, and T. Lasser, "Optical coherence tomography-principles and applications," *Reports Progress Phys.*, vol. 66, p. 239–303, 2003.
- [10] J. M. Schmitt and G. Kumar, "Optical scattering properties of soft tissue: A discrete particle model," *Appl. Opt.*, vol. 37, pp. 2788–2797, 1998.
- [11] W. Drexler and J. G. Fujimoto, "State-of-the-art retinal optical coherence tomography," *Progress Retinal Eye Res.*, vol. 27, pp. 45–88, 2008.
- [12] I.-K. Jang *et al.*, "In vivo characterization of coronary atherosclerotic plaque by use of optical coherence tomography," *Circulation*, vol. 111, pp. 1551–1555, 2005.
- [13] R. K. Wang, L. An, P. Francis, and D. J. Wilson, "Depth-resolved imaging of capillary networks in retina and choroid using ultrahigh sensitive optical microangiography," *Opt. Lett.*, vol. 35, pp. 1467–1469, 2010.
- [14] A. M. Zysk and S. A. Boppart, "Computational methods for analysis of human breast tumor tissue in optical coherence tomography images," *J. Biomed. Opt.*, vol. 11, Sep./Oct. 2006, Art. no. 054015.
- [15] T. M. Lee *et al.*, "Engineered microsphere contrast agents for optical coherence tomography," *Opt. Lett.*, vol. 28, pp. 1546–1548, 2003.
- [16] C. Yang, "Molecular contrast optical coherence tomography: A review," *Photochem. Photobiol.*, vol. 81, pp. 215–237, 2005.
- [17] U. Prabhakar *et al.*, "Challenges and key considerations of the enhanced permeability and retention effect for nanomedicine drug delivery in oncology," *Cancer Res.*, vol. 73, pp. 2412–2417, Apr. 2013.
- [18] W. Cai and X. Chen, "Nanoplatforms for targeted molecular imaging in living subjects," *Small*, vol. 3, pp. 1840–1854, 2007.
- [19] A. L. Oldenburg, B. E. Applegate, J. A. Izatt, and S. A. Boppart, "Molecular OCT contrast enhancement and imaging," in *Optical Coherence Tomography: Technology and Applications*, 1st ed., W. Drexler and J. G. Fujimoto, Eds. New York, NY, USA: Springer, pp. 713–756.
- [20] S. A. Boppart, A. L. Oldenburg, C. Xu, and D. L. Marks, "Optical probes and techniques for molecular contrast enhancement in coherence imaging," *J. Biomed. Opt.*, vol. 10, Jul./Aug. 2005, Art. no. 41208.
- [21] J. F. Schenck, "The role of magnetic susceptibility in magnetic resonance imaging: MRI magnetic compatibility of the first and second kinds," *Med. Phys.*, vol. 23, pp. 815–850, 1996.
- [22] M. A. Choma, A. K. Ellerbee, C. Yang, and J. A. Izatt, "Spectral domain phase microscopy," presented at the *Biomedical Topical Meeting*, Miami Beach, FL, USA, 2004, Paper SC5.
- [23] O. Clement, N. Siauve, C.-A. Cuénod, and G. Frija, "Liver imaging with ferumoxides (feridex (R)): Fundamentals, controversies, and practical aspects," *Topics Magnetic Resonance Imaging*, vol. 9, pp. 167–182, 1998.
- [24] K. Woo *et al.*, "Easy synthesis and magnetic properties of iron oxide nanoparticles," *Chemistry Mater.*, vol. 16, pp. 2814–2818, 2004.
- [25] J. Tang, M. Myers, K. A. Bosnick, and L. E. Brus, "Magnetite Fe<sub>3</sub>O<sub>4</sub> nanocrystals: Spectroscopic observation of aqueous oxidation kinetics," *J. Phys. Chem. B*, vol. 107, pp. 7501–7506, 2003.
- [26] D. E. Sosnovik, M. Nahrendorf, and R. Weissleder, "Magnetic nanoparticles for MR imaging: Agents, techniques and cardiovascular applications," *Basic Res. Cardiol.*, vol. 103, pp. 122–130, 2008.
- [27] C.-C. Huang *et al.*, "New insight on optical and magnetic Fe<sub>3</sub>O<sub>4</sub> nanoclusters promising for near infrared theranostic applications," *Nanoscale*, vol. 7, pp. 12689–12697, 2015.
- [28] F. T. Nguyen *et al.*, "Magnetic protein microspheres as dynamic contrast agents for magnetomotive optical coherence tomography," *Proc. SPIE*, vol. 6867, 2008, Art. no. 68670F.
- [29] A. L. Oldenburg, V. Crecea, S. A. Rinne, and S. A. Boppart, "Phase-resolved magnetomotive OCT for imaging nanomolar concentrations of magnetic nanoparticles in tissues," *Opt. Express*, vol. 16, pp. 11525–11539, Jul. 2008.
- [30] A. L. Oldenburg *et al.*, "Magnetic and contrast properties of labeled platelets for magnetomotive optical coherence tomography," *Biophys. J.*, vol. 99, pp. 2374–2383, Oct. 2010.
- [31] J.-P. Fortin *et al.*, "Size-sorted anionic iron oxide nanomagnets as colloidal mediators for magnetic hyperthermia," *J. Amer. Chem. Soc.*, vol. 129, pp. 2628–2635, 2007.
- [32] A. Ahmad, J. Kim, N. D. Shemonski, M. Marjanovic, and S. A. Boppart, "Volumetric full-range magnetomotive optical coherence tomography," *J. Biomed. Opt.*, vol. 19, Dec. 2014, Art. no. 126001.
- [33] J. Kim, A. Ahmad, and S. A. Boppart, "Dual-coil magnetomotive optical coherence tomography for contrast enhancement in liquids," *Opt. Express*, vol. 21, pp. 7139–7147, Mar. 2013.
- [34] J. Koo *et al.*, "Pulsed magneto-motive optical coherence tomography for remote cellular imaging," *Opt. Lett.*, vol. 37, pp. 3714–3716, 2012.
- [35] G. J. Higby, "Gold in medicine," *Gold Bull.*, vol. 15, pp. 130–140, 1982.
- [36] N. M. Schaublin *et al.*, "Surface charge of gold nanoparticles mediates mechanism of toxicity," *Nanoscale*, vol. 3, pp. 410–420, 2011.
- [37] Y. Yguerabide and E. E. Yguerabide, "Light-scattering submicroscopic particles as highly fluorescent analogs and their use as tracer labels in clinical and biological applications: I. Theory," *Analytical Biochem.*, vol. 262, pp. 137–156, 1998.
- [38] X. Huang, I. H. El-Sayed, W. Qian, and M. A. El-Sayed, "Cancer cell imaging and photothermal therapy in the near-infrared region by using gold nanorods," *J. Amer. Chem. Soc.*, vol. 128, pp. 2115–2120, 2006.
- [39] S. E. Skrabalak *et al.*, "Gold nanocages: Synthesis, properties, and applications," *Accounts Chem. Res.*, vol. 41, pp. 1587–1595, Dec. 2008.
- [40] J. Aizpurua *et al.*, "Optical properties of gold nanorings," *Phys. Rev. Lett.*, vol. 90, 2003, Art. no. 057401.
- [41] C. Loo *et al.*, "Nanoshell-enabled photonics-based imaging and therapy of cancer," *Technol. Cancer Res. Treatment*, vol. 3, pp. 33–40, Feb. 2004.
- [42] A. L. Oldenburg *et al.*, "Motility-, autocorrelation-, and polarization-sensitive optical coherence tomography discriminates cells and gold nanorods within 3D tissue cultures," *Opt. Lett.*, vol. 38, pp. 2923–2926, Aug. 2013.
- [43] W. E. Al Rwashdeh *et al.*, "Differential contrast of gold nanorods in dual-band OCT using spectral multiplexing," *J. Nanoparticle Res.*, vol. 17, 2015, Art. no. 138.
- [44] A. L. Oldenburg, M. N. Hansen, D. A. Zweifel, A. Wei, and S. A. Boppart, "Plasmon-resonant gold nanorods as low backscattering albedo contrast agents for optical coherence tomography," *Opt. Express*, vol. 14, pp. 6724–6738, Jul. 2006.
- [45] C. F. Bohren and D. R. Huffman, *Absorption and Scattering of Light by Small Particles*. New York, NY, USA: Wiley, 2008.
- [46] C. Sonnichsen *et al.*, "Drastic reduction of plasmon damping in gold nanorods," *Phys. Rev. Lett.*, vol. 88, pp. 077402–077402, 2002.
- [47] H. Cang *et al.*, "Gold nanocages as contrast agents for spectroscopic optical coherence tomography," *Opt. Lett.*, vol. 30, pp. 3048–3050, Nov. 2005.
- [48] U. Morgner *et al.*, "Spectroscopic optical coherence tomography," *Opt. Lett.*, vol. 25, pp. 111–113, 2000.
- [49] L. Thrane, H. T. Yura, and P. E. Andersen, "Analysis of optical coherence tomography systems based on the extended Huygens–Fresnel principle," *J. Opt. Soc. Amer. A*, vol. 17, pp. 484–490, 2000.

- [50] W.-F. Cheong, S. A. Prahl, and A. J. Welch, "A review of the optical properties of biological tissues," *IEEE J. Quantum Electron.*, vol. 26, no. 12, pp. 2166–2185, Dec. 1990.
- [51] C. Xu, D. Marks, M. Do, and S. Boppart, "Separation of absorption and scattering profiles in spectroscopic optical coherence tomography using a least-squares algorithm," *Opt. Express*, vol. 12, pp. 4790–4803, 2004.
- [52] A. L. Oldenburg, M. N. Hansen, A. Wei, and S. A. Boppart, "Plasmon-resonant gold nanorods provide spectroscopic OCT contrast in excised human breast tumors," in *Proc. SPIE*, vol. 6867, 2008, pp. 68670E–1–68670E-10.
- [53] C. Xu, J. Ye, D. L. Marks, and S. A. Boppart, "Near-infrared dyes as contrast-enhancing agents for spectroscopic optical coherence tomography," *Opt. Lett.*, vol. 29, pp. 1647–1649, 2004.
- [54] C. Yang, L. E. McGuckin, J. D. Simon, M. A. Choma, B. E. Applegate, and J. A. Izatt, "Spectral triangulation molecular contrast optical coherence tomography with indocyanine green as the contrast agent," *Opt. Lett.*, vol. 29, pp. 2016–2018, 2004.
- [55] T. Weyand *et al.*, "Differential contrast of gold nanorods in dual-band OCT using spectral multiplexing," *J. Nanoparticle Res.*, vol. 17, pp. 1–11, 2015.
- [56] S. J. Oldenburg, J. B. Jackson, S. L. Westcott, and N. Halas, "Infrared extinction properties of gold nanoshells," *Appl. Phys. Lett.*, vol. 75, pp. 2897–2899, 1999.
- [57] K. Sokolov *et al.*, "Real-time vital optical imaging of precancer using anti-epidermal growth factor receptor antibodies conjugated to gold nanoparticles," *Cancer Res.*, vol. 63, pp. 1999–2004, 2003.
- [58] D. C. Adler, S. W. Huang, R. Huber, and J. G. Fujimoto, "Photothermal detection of gold nanoparticles using phase-sensitive optical coherence tomography," *Opt. Express*, vol. 16, pp. 4376–4393, Mar. 2008.
- [59] M. C. Skala, M. J. Crow, A. Wax, and J. A. Izatt, "Photothermal optical coherence tomography of epidermal growth factor receptor in live cells using immunotargeted gold nanospheres," *Nano Lett.*, vol. 8, pp. 3461–3467, 2008.
- [60] C. Pache *et al.*, "Fast three-dimensional imaging of gold nanoparticles in living cells with photothermal optical lock-in optical coherence microscopy," *Opt. Express*, vol. 20, pp. 21385–21399, Sep. 2012.
- [61] J. M. Tucker-Schwartz, M. Lapierre-Landry, C. A. Patil, and M. C. Skala, "Photothermal optical lock-in optical coherence tomography for in vivo imaging," *Biomed. Opt. Express*, vol. 6, pp. 2268–2282, Jun. 2015.
- [62] D. A. Boas, K. K. Bizheva, and A. M. Siegel, "Using dynamic low-coherence interferometry to image Brownian motion within highly scattering media," *Opt. Lett.*, vol. 23, pp. 319–321, Mar. 1998.
- [63] J. Lee, W. Wu, J. Y. Jiang, B. Zhu, and D. A. Boas, "Dynamic light scattering optical coherence tomography," *Opt. Express*, vol. 20, pp. 22262–22277, 2012.
- [64] R. K. Chhetri, K. A. Kozek, A. C. Johnston-Peck, J. B. Tracy, and A. L. Oldenburg, "Imaging three-dimensional rotational diffusion of plasmon resonant gold nanorods using polarization-sensitive optical coherence tomography," *Phys. Rev. E*, vol. 83, 2011, Art. no. 040903.
- [65] R. K. Chhetri *et al.*, "Probing biological nanotopology via diffusion of weakly constrained plasmonic nanorods with optical coherence tomography," *Proc. Nat. Acad. Sci. USA*, vol. 111, pp. E4289–E4297, Oct. 2014.
- [66] A. L. Oldenburg *et al.*, "Magnetic contrast agents for optical coherence tomography," *Proc. SPIE*, vol. 5316, pp. 91–98, 2004.
- [67] A. L. Oldenburg, J. R. Gunther, and S. A. Boppart, "Imaging magnetically labeled cells with magnetomotive optical coherence tomography," *Opt. Lett.*, vol. 30, pp. 747–749, Apr. 2005.
- [68] A. L. Oldenburg, F. J. J. Toublan, K. S. Suslick, A. Wei, and S. A. Boppart, "Magnetomotive contrast for in vivo optical coherence tomography," *Opt. Express*, vol. 13, pp. 6597–6614, Aug. 2005.
- [69] D. P. Davé and T. E. Milner, "Optical low-coherence reflectometer for differential phase measurement," *Opt. Lett.*, vol. 25, pp. 227–229, 2000.
- [70] J. Oh, M. D. Feldman, J. Kim, H. W. Kang, P. Sanghi, and T. E. Milner, "Magneto-motive detection of tissue-based macrophages by differential phase optical coherence tomography," *Lasers Surg. Med.*, vol. 39, pp. 266–272, Mar. 2007.
- [71] J. Oh *et al.*, "Detection of macrophages in atherosclerotic tissue using magnetic nanoparticles and differential phase optical coherence tomography," *J. Biomed. Opt.*, vol. 13, Sep./Oct. 2008, Art. no. 054006.
- [72] M. Choma, M. Sarunic, C. Yang, and J. Izatt, "Sensitivity advantage of swept source and Fourier domain optical coherence tomography," *Opt. Express*, vol. 11, pp. 2183–2189, 2003.
- [73] R. Leitgeb, C. Hitzenberger, and A. Fercher, "Performance of fourier domain vs. time domain optical coherence tomography," *Opt. Express*, vol. 11, pp. 889–894, 2003.
- [74] V. Crecea, A. L. Oldenburg, T. S. Ralston, and S. A. Boppart, "Phase-resolved spectral-domain magnetomotive optical coherence tomography - art. no. 64291X," *Proc. SPIE*, vol. 6429, pp. X4291–X4291, 2007.
- [75] P. Cimalla *et al.*, "Imaging of nanoparticle-labeled stem cells using magnetomotive optical coherence tomography, laser speckle reflectometry, and light microscopy," *J. Biomed. Opt.*, vol. 20, Mar. 2015, Art. no. 036018.
- [76] X. Liang, S. G. Adie, R. John, and S. A. Boppart, "Dynamic spectral-domain optical coherence elastography for tissue characterization," *Opt. Express*, vol. 18, pp. 14183–14190, 2010.
- [77] V. Crecea, A. Ahmad, and S. A. Boppart, "Magnetomotive optical coherence elastography for microrheology of biological tissues," *J. Biomed. Opt.*, vol. 18, Dec. 2013, Art. no. 121504.
- [78] V. Crecea, B. W. Graf, T. Kim, G. Popescu, and S. A. Boppart, "High resolution phase-sensitive magnetomotive optical coherence microscopy for tracking magnetic microbeads and cellular mechanics," *IEEE J. Sel. Top. Quantum Electron.*, vol. 20, no. 2, Mar./Apr. 2014, Art. no. 6800907.
- [79] A. Ahmad, J. Kim, N. A. Sobh, N. D. Shemonski, and S. A. Boppart, "Magnetomotive optical coherence elastography using magnetic particles to induce mechanical waves," *Biomed. Opt. Express*, vol. 5, pp. 2349–2361, Jul. 2014.
- [80] A. Ahmad *et al.*, "Mechanical contrast in spectroscopic magnetomotive optical coherence elastography," *Phys. Med. Biol.*, vol. 60, pp. 6655–6668, Sep. 2015.
- [81] A. L. Oldenburg and S. A. Boppart, "Resonant acoustic spectroscopy of soft tissues using embedded magnetomotive nanotransducers and optical coherence tomography," *Phys. Med. Biol.*, vol. 55, pp. 1189–1201, Feb. 2010.
- [82] A. L. Oldenburg *et al.*, "Imaging and elastometry of blood clots using magnetomotive optical coherence tomography and labeled platelets," *IEEE J. Sel. Topics Quantum Electron.*, vol. 18, no. 3, p. 1100–1109, May/Jun. 2012.
- [83] A. L. Oldenburg, D. Spivak, G. Wu, F. Tsui, and T. H. Fischer, "Optimizing magnetomotive contrast of SPIO-labeled platelets for thrombosis imaging in optical coherence tomography," *Proc. SPIE*, vol. 8213, 2012, Art. no. 82131N.
- [84] R. John and S. A. Boppart, "Magnetomotive molecular Nanoprobes," *Current Medicinal Chem.*, vol. 18, pp. 2103–2114, May 2011.
- [85] R. S. Molday and D. Mackenzie, "Immunospecific ferromagnetic iron-dextran reagents for the labeling and magnetic separation of cells," *J. Immunological Methods*, vol. 52, pp. 353–367, 1982.
- [86] R. John *et al.*, "In vivo magnetomotive optical molecular imaging using targeted magnetic nanoprobes," *Proc. Nat. Academy Sci. USA*, vol. 107, pp. 8085–8090, May 2010.
- [87] J. Yang *et al.*, "Ultrasensitive detection and molecular imaging with magnetic nanoparticles," *Analyst*, vol. 133, pp. 154–160, 2008.
- [88] A. L. Oldenburg, V. Crecea, S. A. Rinne, and S. A. Boppart, "Phase-resolved magnetomotive OCT for imaging nanomolar concentrations of magnetic nanoparticles in tissues," *Opt. Express*, vol. 16, pp. 11525–11539, Jul. 2008.
- [89] R. John, F. T. Nguyen, K. J. Kolbeck, E. J. Chaney, M. Marjanovic, K. S. Suslick, and S. A. Boppart, "Targeted multifunctional multimodal protein-shell microspheres as cancer imaging contrast agents," *Mol. Imag. Biol.*, vol. 14, pp. 17–24, Feb. 2012.
- [90] J. Kim *et al.*, "Magnetomotive optical coherence tomography for the assessment of atherosclerotic lesions using alpha(v)beta(3) integrin-targeted microspheres," *Mol. Imag. Biol.*, vol. 16, pp. 36–43, Feb. 2014.
- [91] H. Maeda, J. Fang, T. Inutsuka, and Y. Kitamoto, "Vascular permeability enhancement in solid tumor: Various factors, mechanisms involved and its implications," *Int. Immunopharmacol.*, vol. 3, pp. 319–328, 2003.
- [92] J. G. White, "Platelets are coverocytes, not phagocytes: Uptake of bacteria involves channels of the open canalicular system," *Platelets*, vol. 16, pp. 121–131, 2005.
- [93] K. Jurk and B. E. Kehrel, "Platelets: Physiology and biochemistry," *Semin. Thromb. Hemost.*, vol. 31, pp. 381–392, 2004.
- [94] A. Jordan, R. Scholz, P. Wust, H. Föhling, and R. Felix, "Magnetic fluid hyperthermia (MFH): Cancer treatment with AC magnetic field induced excitation of biocompatible superparamagnetic nanoparticles," *J. Magnetism Magn. Mater.*, vol. 201, pp. 413–419, 1999.

- [95] J. Wang *et al.*, "Detection of magnetic particles in live DBA/2J mouse eyes using magnetomotive optical coherence tomography," *Eye Contact Lens-Sci. Clin. Practice*, vol. 36, pp. 346–351, Nov. 2010.
- [96] J. Wang, A. Aljohani, T. Carreon, G. Gregori, and S. K. Bhattacharya, "In vivo quantification of cochlin in glaucomatous DBA/2J mice using optical coherence tomography," *Sci. Rep.*, vol. 5, Jun. 2015, Art. no. 11095.
- [97] R. K. Chhetri, J. Carpenter, R. Superfine, S. H. Randell, and A. L. Oldenburg, "Magnetomotive optical coherence elastography for relating lung structure and function in cystic fibrosis," *Proc. SPIE*, vol. 7554, 2010, Art. no. 755420.
- [98] X. Huang and M. A. El-Sayed, "Gold nanoparticles: Optical properties and implementations in cancer diagnosis and photothermal therapy," *J. Adv. Res.*, vol. 1, pp. 13–28, 2010.
- [99] J. Perezjuste, I. Pastorizasantos, L. Lizmarzan, and P. Mulvaney, "Gold nanorods: Synthesis, characterization and applications," *Coordination Chem. Rev.*, vol. 249, pp. 1870–1901, 2005.
- [100] L. L. Ma *et al.*, "Small multifunctional nanoclusters (Nanoroses) for targeted cellular imaging and therapy," *ACS Nano*, vol. 3, pp. 2686–2696, Sep. 2009.
- [101] F. Hao, C. L. Nehl, J. H. Hafner, and P. Nordlander, "Plasmon resonances of a gold nanostar," *Nano Lett.*, vol. 7, pp. 729–732, Mar. 2007.
- [102] M. Wei *et al.*, "Differential absorption optical coherence tomography with strong absorption contrast agents of gold nanorods," *Frontiers Optoelectron. China*, vol. 2, pp. 141–145, 2009.
- [103] Y. Jia *et al.*, "Spectral fractionation detection of gold nanorod contrast agents using optical coherence tomography," *Opt. Express*, vol. 23, pp. 4212–4225, Feb. 2015.
- [104] C. H. Yang *et al.*, "Spectral triangulation molecular contrast optical coherence tomography with indocyanine green as the contrast agent," *Opt. Lett.*, vol. 29, pp. 2016–2018, Sep. 2004.
- [105] A. M. Gobin *et al.*, "Near-infrared resonant nanoshells for combined optical imaging and photothermal cancer therapy," *Nano Lett.*, vol. 7, pp. 1929–1934, Jul. 2007.
- [106] M. Kirillin *et al.*, "Contrasting properties of gold nanoshells and titanium dioxide nanoparticles for optical coherence tomography imaging of skin: Monte Carlo simulations and in vivo study," *J. Biomed. Opt.*, vol. 14, Mar./Apr. 2009, Art. no. 021017.
- [107] E. V. Zagaynova *et al.*, "Contrasting properties of gold nanoparticles for optical coherence tomography: Phantom, in vivo studies and Monte Carlo simulation," *Phys. Med. Biol.*, vol. 53, pp. 4995–5009, Sep. 2008.
- [108] U. S. Dinish *et al.*, "Optimized synthesis of PEG-Encapsulated gold nanorods for improved stability and its application in OCT imaging with enhanced contrast," *Plasmonics*, vol. 8, pp. 591–598, 2012.
- [109] A. de la Zerda *et al.*, "Optical coherence contrast imaging using gold nanorods in living mice eyes," *Clin. Exp. Ophthalmol.*, vol. 43, pp. 358–366, May/June. 2015.
- [110] O. Bibikova *et al.*, "Optical properties of plasmon-resonant bare and silica-coated nanostars used for cell imaging," *J. Biomed. Opt.*, vol. 20, Jul. 2015, Art. no. 076017.
- [111] F. Zhou *et al.*, "Influence of nanoparticles accumulation on optical properties of human normal and cancerous liver tissue in vitro estimated by OCT," *Phys. Med. Biol.*, vol. 60, pp. 1385–1397, Feb. 2015.
- [112] H. Y. Tseng *et al.*, "Au nanorings for enhancing absorption and backscattering monitored with optical coherence tomography," *Nanotechnology*, vol. 21, Jul. 2010, Art. no. 295102.
- [113] J. Xi, Y. Chen, and X. Li, "Characterizing optical properties of nano contrast agents by using cross-referencing OCT imaging," *Biomed. Opt. Express*, vol. 4, pp. 842–851, Jun. 2013.
- [114] B. Wang *et al.*, "Gold nanorods as a contrast agent for Doppler optical coherence tomography," *PLoS One*, vol. 9, 2014, Art. no. e90690.
- [115] M. A. Sirotkina *et al.*, "OCT-guided laser hyperthermia with passively tumor-targeted gold nanoparticles," *J. Biophoton.*, vol. 3, pp. 718–727, Oct. 2010.
- [116] A. J. Coughlin *et al.*, "Gadolinium-conjugated gold nanoshells for multimodal diagnostic imaging and photothermal cancer therapy," *Small*, vol. 10, pp. 556–565, Feb. 2014.
- [117] Y. Ponce de León, J. L. Pichardo-Molina, and N. Alcalá Ochoa, "Growth kinetics of concave nanocubes studied by optical coherence tomography," *Plasmonics*, vol. 9, pp. 907–915, 2014.
- [118] A. L. Oldenburg, C. Xu, and S. A. Bopp, "Spectroscopic optical coherence tomography and microscopy," *IEEE J. Sel. Top. Quantum Electron.*, vol. 13, no. 6, pp. 1629–1640, Nov./Dec. 2007.
- [119] A. L. Oldenburg, M. N. Hansen, T. S. Ralston, A. Wei, and S. A. Bopp, "Imaging gold nanorods in excised human breast carcinoma by spectroscopic optical coherence tomography," *J. Mater. Chem.*, vol. 19, Jan. 2009, Art. no. 6407.
- [120] C. Zhou *et al.*, "Photothermal optical coherence tomography in vivo human breast tissues using gold nanoshells," *Opt. Lett.*, vol. 35, pp. 700–702, Mar. 2010.
- [121] A. S. Paranjape *et al.*, "Depth resolved photothermal OCT detection of macrophages in tissue using nanorose," *Biomed. Opt. Express*, vol. 1, pp. 2–16, Aug. 2010.
- [122] P. Xiao *et al.*, "Detection of pH-induced aggregation of "smart" gold nanoparticles with photothermal optical coherence tomography," *Opt. Lett.*, vol. 38, pp. 4429–4432, Nov. 2013.
- [123] T. T. Chi *et al.*, "Photothermal optical coherence tomography based on the localized surface plasmon resonance of Au nanoring," *Opt. Express*, vol. 22, pp. 11754–11769, May 2014.
- [124] A. Nahas, M. Varna, E. Fort, and A. C. Boccara, "Detection of plasmonic nanoparticles with full field-OCT: Optical and photothermal detection," *Biomed. Opt. Express*, vol. 5, pp. 3541–3546, Oct. 2014.
- [125] J. Kalkman, R. Sprik, and T. G. van Leeuwen, "Path-length-resolved diffusive particle dynamics in spectral-domain optical coherence tomography," *Phys. Rev. Lett.*, vol. 105, 2010, Art. no. 198302.
- [126] C. K. Lee *et al.*, "Characterizing the localized surface plasmon resonance behaviors of Au nanorings and tracking their diffusion in bio-tissue with optical coherence tomography," *Biomed. Opt. Express*, vol. 1, pp. 1060–1074, Nov. 2010.
- [127] K. B. Mehta and N. Chen, "Plasmonic chiral contrast agents for optical coherence tomography: Numerical study," *Opt. Express*, vol. 19, pp. 14903–14912, Aug. 2011.



**Amy L. Oldenburg** received the B.S. degree in applied physics from the California Institute of Technology, Pasadena, CA, USA, in 1995, and the Ph.D. degree in physics from the University of Illinois at Urbana-Champaign, Champaign, IL, USA, in 2001.

From 2001 to 2008, she was a Postdoctoral Research Associate and subsequently a Senior Research Scientist at the Beckman Institute, University of Illinois at Urbana-Champaign, where she invented magnetomotive OCT, and investigated a variety of OCT contrast agents for biomedical applications including

breast cancer molecular imaging and elastography. Since 2008, she has been directing the Coherence Imaging Laboratory, Department of Physics and Astronomy, University of North Carolina at Chapel Hill, Chapel Hill, NC, as an Assistant and subsequently an Associate Professor.

Dr. Oldenburg received the NSF CAREER Award in 2014. She became a Senior Member of OSA in 2013 and a Senior Member of SPIE in 2011.

**Richard L. Blackmon** received the B.S. degree in electrical engineering in 2009 and the Ph.D. degree in optical science and engineering in 2013, both from the University of North Carolina at Charlotte, Charlotte, NC, USA. From 2008 to 2013, he was a Research Assistant in the Biomedical Optics Laboratory, Department of Physics and Optical Science, where he investigated laser therapeutics in urology. Since 2013, he has been a Postdoctoral Research Associate in the Coherence Imaging Laboratory, Department of Physics and Astronomy, University of North Carolina at Chapel Hill, Chapel Hill, NC, where he investigates OCT imaging of diffusing gold nanoparticles for elastography of diseased tissue.

Dr. Blackmon received the NSF Graduate Research Fellowship in 2010 and the UNC Charlotte Graduate Life Fellowship in 2013. He is currently a Member of OSA and SPIE.

**Justin M. Sierchio** received the B.S., M.S., and Ph.D. degrees in optical sciences and engineering from the College of Optical Sciences, University of Arizona, Tucson, AZ, USA, in 2006, 2008, and 2014, respectively. He also served as a Principle Research Specialist at the University of Arizona, working on designs of diabetic foot wound recovery sensors and point-of-care monitoring devices. Since 2015, he has been a Postdoctoral Research Associate at the Optical Coherence Imaging Laboratory, Department of Physics and Astronomy, University of North Carolina at Chapel Hill, Chapel Hill, NC, USA, investigating development of magnetomotive ultrasound techniques for thrombosis and atherosclerosis characterization. He is a Member of SPIE.